# On the Electromagnetic Performance Prediction of Turbo Synchronous Condensers Based on Wound-Field Flux Switching Machine Design

Udochukwu B. Akuru, *Senior Member, IEEE*, Mkhululi Mabhula, *Member, IEEE*, and Maarten J. Kamper, *Senior Member, IEEE*

***Abstract*—The revival of the old synchronous condenser (SC) technology is presently occurring. Hence, this study is proposed on the electromagnetic design and evaluation of turbo wound-field flux switching machines (WF-FSMs) for SC operation, for the first time. Unlike classical wound-field rotating machines, WF-FSMs do not need brushless exciters while possessing a robust topology. A design process based on the frozen permeability technique in static 2-D finite element analysis script-based package, which enhances both iterative and analytic adjudications, is proposed to accurately predict the SC operation. To attain the specific design requirements (∼300 MVAR, 16 kV), a global-optimized model (GOM) of the SC machine is obtained through a stochastic optimization process involving multiple objectives. Based on the GOM, simple torque ripple minimization techniques are implemented, from which a final benchmark design is selected. The proposed SC analytical design procedure is then tested and the expected V-curves clearly obtained. The whole design approach is further verified by experimenting on a small-scale prototype, which when synchronized to the grid, confirms the novelty and feasibility of the proposed SC design and operation.**

***Index Terms*—Analytical model, finite element analyses (FEA), frozen permeability (FP), optimization, synchronous condenser (SC), wound-field flux switching machine (WF-FSM).**

## I. Introduction

THE SYNCHRONOUS condenser (SC) technology, used for leveraging power flow in power systems, is as old as the electrical power network [1], [2]. From the onset, it has served mainly as reactive power generator, voltage stabilizer, and rate of change of frequency (ROCOF) arrestor in ac power networks. The original technology is based predominantly on rotating wound-rotor synchronous machines up until the early 1970s, when the advent of power electronic devices such as static reactive power (VAR) compensator—SVC, shunt compensator—STATCOM, flexible ac transmission systems (FACTS), etc., made them obsolete. Static compensator devices were considered cheaper with no moving parts [1].

However, in recent times, a revival of the old SC condenser technology has blossomed due to growing integration of renewable energy into the energy mix, among others [3]–[5]. It is understood that static compensator devices are somehow constrained if meant to address the disruptive demands of the modern grid because of limited injection of reactive power, low inertia response, and poor voltage regulation, which implies that its so-called short-circuit ratio (SCR) and grid inertia performance can be dismal [1], [2], [4]–[6]. To this end, the old rotating SCs are being preferred today because unlike modern STATCOMs, they provide high rotational inertia and short-circuit MVA capabilities [3], [6], [7].

In the literature, it is commonly noted that rotating SCs are dominated by turbo synchronous machines with ratings usually in excess of 100 MVAR [2], [5], [8], [9], although there is recent emergence of smaller units to account for both transmission modularity and microgrid resilience [1], [3]. To this end, it is difficult to find studies that have deliberately focused on the electromagnetic design, e.g., finite element analysis (FEA), complete with optimization of such turbo machines, with emphasis on important reference design data on dimensional and performance characteristics. Attempts were made in [8]–[10] mainly on FEA, but these studies do not provide the exact machine parameters, nor do they make mention of techniques required for setting up the design process.

Therefore, this study is an attempt to establish the design procedure for the electromagnetic modeling and performance prediction of turbo SCs with well-described analytical and FEA procedures, based on the wound-field flux switching machine (WF-FSM) technology. To the best of the authors' knowledge, and apart from their recent conference paper [11], such a research adventure is yet to be accomplished for SC designs in the turbo range, especially on the implementation

Manuscript received August 26, 2020; revised December 14, 2020 and March 15, 2021; accepted April 25, 2021. Date of publication May 17, 2021; date of current version July 16, 2021. Paper 2020-EMC-1358.R2, presented at the 2019 Energy Conversion Congress & Exposition, Baltimore, MD, USA, Sep. 29–Oct. 3, and approved for publication in the IEEE Transactions on Industry Applications by the Electric Machines Committee of the IEEE Industry Applications Society. This research was financially supported by the Centre for Renewable and Sustainable Energy Studies (CRSES) at Stellenbosch University, Stellenbosch, South Africa, and the Department of Science and Innovation (DSI) in South Africa. *(Corresponding author: Udochukwu Bola Akuru.)*

Udochukwu B. Akuru is with the Department of Electrical Engineering, Tshwane University of Technology, Pretoria 0183, South Africa, with the Department of Electrical and Electronic Engineering, Stellenbosch University, Stellenbosch 7600, South Africa, and also with the Department of Electrical Engineering, University of Nigeria, Nsukka 410001, Nigeria (e-mail: akuruub@tut.ac.za).

Mkhululi Mabhula and Maarten J. Kamper are with the the Department of Electrical and Electronic Engineering, Stellenbosch University, Stellenbosch 7600, South Africa (e-mail: mabhulamkhululi@gmail.com; kamper@sun.ac.za).

Color versions of one or more figures in this article are available at https://doi.org/10.1109/TIA.2021.3080668.

Digital Object Identifier 10.1109/TIA.2021.3080668

TABLE I
CHARACTERIZATION AND DESIGN SPECIFICATIONS

| Parameters | Values |
|---|---|
| Reactive power, $Q$ | 300 MVAR |
| Rated line voltage, $V_L$ | 16 kV |
| Rated speed, $n$ | 300 r/min |
| Phase number, $m$ | 3 |
| Number of stator slots, $N_s$ | 12 |
| Number of rotor teeth, $N_r$ | 10 |

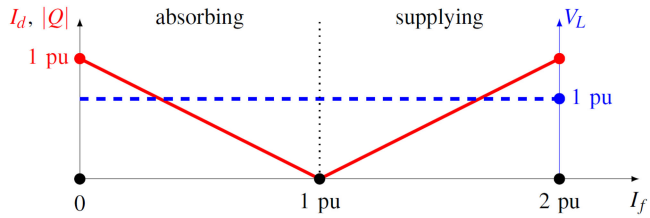


Fig. 1. Sample V-curve of SC operating points.

of WF-FSMs for SC operation. The expectation is that the design approach herein proposed is not only simplified, but also enhanced. Additionally, the intention of the authors is to evaluate the proposed WF-FSM SC concept using a small-scale experimental prototype. The experimental process of the SC technology operation, which is usually preceded by direct-grid synchronization, is also novel to this study.

Meanwhile, it is important to stress that the WF-FSM is a synchronous machine variant, which existed for long but have only recently been revived due to increased awareness on its inherent qualities such as its stator-mounted wound-field electromagnets and robust salient rotor structures [12], [13]. Consequently, it has been nominated for this study because: i) it does not need brushes and slip rings for its dc field excitation due to stator-mounted coils, ii) it exhibits easy thermal management for the same reason as (i), and (iii) it has a robust rotor feature. In addition, due to high split ratio characteristics of WF-FSMs [14], the desired rotational inertia performance for the SC operation is expected to be boosted, among others.

On the other hand, it is also important not to shy away from the fact that notable challenges are posed by the proposed design. For example, the possibility of high dc winding induced voltage pulsations in the wound-field coils; but this has been addressed accordingly in [15] by simple rotor skewing. Also, being the most dominant of losses [11], the accurate prediction of the core losses should be of great concern. To account for these uncertainties, 3-D transient FEA evaluation is undertaken on the proposed turbo SC in a steady state to verify their exigencies on the performance prediction. But to facilitate the study, some assumptions have been attributed in the design of the proposed turbo SC, including the nonsolicitation of the necessary cooling and excitation strategies. As regards the thermal and mechanical design finesse, a disclaimer is hereby made to state that it is beyond the scope of this study. Also, the transient response of the proposed SC under grid-fault conditions, as well as high proximity and skin effects present in form-wound machines, which may be exacerbated due to the turbo-sized SC [16], are not considered in this study.

To achieve the objectives of the study, an outline of the machine specifications is given in Table I. In the rest of the article, an analytical procedure of the electromagnetic design and performance prediction in SC mode is first proposed with the aid of a static 2-D FEA package [17], complemented with end-winding effects. To attain the design requirements, the developed analytical SC model is globally optimized and an optimum design benchmark is selected and evaluated. Finally, an existing small-scale WF-FSM laboratory prototype is experimented at the end of the study as a proof-of-the-concept.

## II. REVISITING THE CONCEPTUAL MODEL

Based on Table I, it should be noted that a 3-phase 12-slots/10-pole (12/10) WF-FSM has been selected for the study. This preference is because, in SC design, maintaining smooth voltage profile, i.e., low voltage harmonic, and the need for high inertia constant ($H$), are necessary preconditions [4], [18]. Hence, for improved grid integration while at the same time promising a high $H$-value, the 12/10 topology presents the best three-phase option due to highest winding factor, presence of symmetrical back-EMF waveforms and balanced magnetic force as well as the least number of rotor poles, which translates to highest possible mechanical speed [19].

The development of the conceptual model (CM), with its main design parameters, has been outlined in [11], and is not rehashed in this paper version for brevity. Meanwhile, the main operating points of any SC are predicted as shown in Fig. 1. Hence, based on Table I, one would expect that should $V_L = 16$ kV, at the main loading regimes of $I_f = 0$, 1 and 2 p.u. (rated), $Q$ should be 300, 0, and –300 MVAR, respectively.

In Section VI, the global design optimization is initiated, which resulted in a global optimized machine (GOM). GOM is produced retrospectively after applying the analytical procedure first developed for predicting the main SC operating regimes in Fig. 1. Compared to [11], the formulations presented in Sections III and V are innovative and more precise for the SC performance prediction in terms of the core loss determination, per unit voltage quality, torque ripple calculation, and more importantly, the FEA-FP-iterative analytic method which yields the exact SC characteristic V-curves.

## III. MODELING AND PERFORMANCE CALCULATION OF SC

In this section, the mathematical model of the SC is explained based on which the performance parameters of the SC are accurately determined.

### A. *Steady-State* dq *Voltage Model*

The *dq* stator flux linkages are expressed complete in motor operation as

$$\lambda_d = L_d I_d + L_{dq} I_q + L_{df} I_f \tag{1}$$

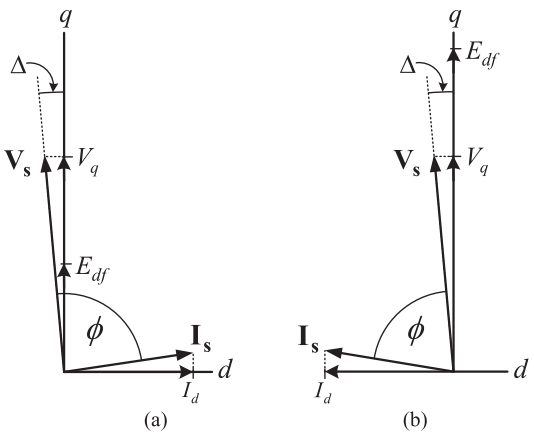


Fig. 2. SC phasor diagrams for different excitation modes. (a) Underexcited ($\Delta < 0$, $\phi$ lags). (b) Overexcited ($\Delta < 0$, $\phi$ leads).

$$\lambda_q = L_q I_q + L_{qd} I_d + L_{qf} I_f \tag{2}$$

where $L_d$ and $L_q$ are the *d*- and *q*-axis self-inductances, $L_{dq}$ and $L_{qd}$ mutual inductances to represent cross coupling between the *d*- and *q*-axis circuits and $L_{df}$ and $L_{qf}$ coupling inductances to represent the magnetic coupling with the field circuit [20]. Using (1) and (2), the steady-state *dq* voltage equations of the SC in motor operation are given by

$$V_d = \sqrt{\tfrac{2}{3}} V_L \sin(\Delta) = R_s I_d - \omega_e L_q I_q - \omega_e L_{qd} I_d - \omega_e L_{qf} I_f \tag{3}$$

$$V_q = \sqrt{\tfrac{2}{3}} V_L \cos(\Delta) = R_s I_q + \omega_e L_d I_d + \omega_e L_{dq} I_q + \omega_e L_{df} I_f \tag{4}$$

where $\Delta$ is very small (due to the almost zero-power SC operation) power angle between the terminal voltage phasor and the *q*-axis (see Fig. 2) and is always negative in motor operation. In (3) and (4), $R_s$ is the phase-winding resistance, $\omega_e$ the electrical angular frequency, and $V_L$ the rms line grid voltage.

We can put (3) and (4) in terms of reactance and induced voltage as

$$\sqrt{\tfrac{2}{3}} V_L \sin(\Delta) = R_s I_d - X_q I_q - \{X_{qd}\} I_d - \{E_{qf}\} \tag{5}$$

$$\sqrt{\tfrac{2}{3}} V_L \cos(\Delta) = R_s I_q + X_d I_d + \{X_{dq}\} I_q + E_{df}\,. \tag{6}$$

The parameters in curly brackets in (5) and (6) are classically ignored in synchronous machine analysis. The above mathematical model is further explained by the phasor diagrams of Fig. 2 for underexcited and overexcited SC operation. From Fig. 2(a), it is seen that in underexcited mode, the current $I_s$ lags the voltage, $V_s$ meaning that reactive power is being absorbed from the grid by the SC, and $\Delta$ is negative. In Fig. 2(b), it is seen that in overexcited mode, $I_s$ leads $V_s$, meaning that reactive power is being supplied to the grid by the SC, while $\Delta$ is still negative.

### B. Power and Loss Calculation

With the *dq* supply voltages and currents of (3) and (4) known for the grid-tie SC, as from Section V, the input power and reactive power of the SC are calculated as

$$P = \frac{3}{2}(V_d I_d + V_q I_q) \tag{7}$$

$$Q = \frac{3}{2}(V_q I_d - V_d I_q). \tag{8}$$

From this, the power factor phase angle shown in Fig. 2 is calculated as

$$\phi = -\tan^{-1}\left(\frac{Q}{P}\right) \tag{9}$$

where a negative sign indicates lagging.

Considering the losses of the SC, the conductor loss of the SC is determined by

$$P_{Cu} = P_{ac} + P_{dc} = \frac{3}{2} R_s (I_d^2 + I_q^2) + R_f I_f^2 \tag{10}$$

where $R_f$ is the total resistance of the field-windings. The core and wind-and-friction losses are lumped together as rotational loss, which is equal to the developed power of the SC as

$$\begin{aligned} P_{ROT} &= P_{Core} + P_{WF} = \omega_s \tau_e \\ &= \tfrac{3}{2} N_r \omega_s (\lambda_d I_q - \lambda_q I_d) \end{aligned} \tag{11}$$

where $\tau_e$ is the electromagnetic torque and $\omega_s$ is the mechanical synchronous speed.

The SC core loss at the solved *dq* and field currents of the SC is determined from a static FEA solution using the Steinmetz empirical formula based on the flux density information in the cores of the SC. The empirical expression is given by

$$P_{Core} = c\, f_k^x (B_t^y M_t + B_{yk}^y M_{yk}) \tag{12}$$

where $B_t$ and $B_{yk}$ are the maximum flux densities in the respective teeth and yoke of the stator and rotor cores, while $M_t$ and $M_{yk}$ are the respective teeth and yoke mass of the stator and rotor. The variables *c*, *x,* and *y* are the Steinmetz coefficients, which depend on the supplied manufacturer's frequency dependent loss characteristics of the core material. The frequency $f_k$ of (12) depends on the stator ('*s*') and rotor ('*r*') components of the WF-FSM, defined respectively as [21]

$$f_s = N_r n/60 \tag{13}$$

$$f_r = N_s n/120 \tag{14}$$

where *n* and $N_s$ are once more, the rotor speed and number of stator slots, respectively.

The wind-and-friction loss $P_{WF}$ of (11) is devised empirically as implicated in [22]. Hence, since $n = 300$ r/min as indicated in Table I, an approximation for $P_{WF}$ is given as

$$P_{WF} \approx \frac{P}{100}(23.23 \times 10^{-9} Q - 0.2) \tag{15}$$

where initially $P$ can be assumed as 0.2% of $Q$ [5].

From above, the total loss of the SC is finally calculated as

$$P_{loss} = P_{Cu} + P_{ROT}. \tag{16}$$

### C. Determining the Voltage and Torque Quality of the SC

The voltage and torque quality of the WF-FSM SC is determined from multiple position-stepping nonlinear static FEA solutions of the SC for given (solved) *dq* ac phase and wound field currents.

With steady-state (fixed) *dq* and field currents, the instantaneous *dq* supply voltages of the SC as a function of the rotor position $\theta$ can be expressed from classical modeling by

$$v_{d(\theta)} = R_s I_d + \frac{\partial \lambda_d}{\partial \theta_e}\omega_e - \omega_e \lambda_{q(\theta)} \tag{17}$$

$$v_{q(\theta)} = R_s I_q + \frac{\partial \lambda_q}{\partial \theta_e}\omega_e + \omega_e \lambda_{d(\theta)}. \tag{18}$$

The flux linkages $\lambda_{d(\theta)}$ and $\lambda_{q(\theta)}$ of (17) and (18) are determined directly from the position-stepped static FEA solutions. To simplify, we ignore the partial differential terms in (17) and (18) in determining of $v_{dq}$. From (17) and (18), we determine the instantaneous voltage vector amplitude as

$$v_{s(\theta)} = \sqrt{v_{d(\theta)}^2 + v_{q(\theta)}^2}. \tag{19}$$

From this, we define and calculate a percentage voltage quality as

$$\Delta v_s = \frac{v_{s(\theta)(\max)} - v_{s(\theta)(\min)}}{V_s} \times 100\,\% \tag{20}$$

where $V_s = v_{s(\theta)(\text{mean})} = 13.06$ kV and where the subscripts "max" and "min" denotes maximum and minimum values.

From the same above position-stepped FEA solutions, the instantaneous torque versus rotor position of the SC is determined by means of the Maxwell stress tensor method. In exactly the way as (20) for the voltage quality, we determine the torque quality of the SC by percentage torque ripple as

$$\Delta \tau_e = \frac{\tau_{e(\theta)(\max)} - \tau_{e(\theta)(\min)}}{T_e} \times 100\,\% \tag{21}$$

where it is taken that $T_e = 300$ MW/(300$\pi$/30) = 9.55 MNm.

### D. Determining the Inertia Constant

Due to its criticality for SC performance operation, the inertia constant $H$ is determined as

$$H = \frac{J\omega_s^2}{2Q} \tag{22}$$

where $J$ the moment of inertia of the rotor mass is defined as

$$J = \frac{M_{rot} R_{rot}^2}{2} \tag{23}$$

with $M_{rot}$ and $R_{rot}$ being the rotor mass and radius, respectively, while taking into account its salient-pole nature.

## IV. Phase Coil Turns and No-Load Field Current

The first step in the simulation of the performance of the grid-tie SC is to determine: i) the correct number of stator turns and ii) the so-called no-load field current of the SC. The determining of these two parameters is briefly considered in this section as also in [11].

### A. Determining the Number of Phase Coil Turns $\mathrm{N_{ph}}$

To determine the number of ac phase coil turns $N_{ph}$, it is necessary to have the SC operating under rated absorbing (positive) reactive power as motor, and at rated voltage, rated current and zero field current. Regarding the latter, it must be noted that the WF-FSM SC can operate at zero field current due to saliency. The rated parameters of the SC are given by

$$\begin{bmatrix} Q \\ V_L \\ I_L \end{bmatrix} = \begin{bmatrix} 300\ \text{MVAR} \\ 16\ \text{kV} \\ 10.83\ \text{kA} \end{bmatrix}. \tag{24}$$

To ensure the condition of (24), the required (rated) $d$-axis current $I_d$ of the SC must be determined, i.e., with the field current $I_f = 0$. To simplify calculations, the following assumptions are made:

1) The volt drop across the stator resistance is ignored, as this is relatively small compared to the rated voltage.
2) It is assumed that $I_q \approx 0$ because the SC has no mechanical load but only a load due to rotational losses.

Both these assumptions will cause very small errors in the determined rated $I_d$. With these assumptions, both $V_d = 0$ and $\Delta = 0$, and thus from (8) and (4) we have

$$I_{d(\text{rated})} = \sqrt{\frac{2}{3}}\frac{Q}{V_L} = 15.31\ \text{kA}. \tag{25}$$

With this current, the induced ac voltage must be equal to the rated supply voltage under the above assumptions. From (1) and (6) under this condition, and knowing $V_L$ and $\omega_e$, the required (rated) $d$-axis stator flux linkage $\lambda_{d(\text{rated})}$ and $d$-axis reactance $X_d$ are calculated as

$$\lambda_{d(\text{rated})} = \sqrt{\frac{2}{3}}\frac{V_L}{\omega_e} = 41.58\ \text{Wb} - \text{turns}$$

$$X_d = \sqrt{\frac{2}{3}}\frac{V_L}{I_{d(\text{rated})}} = 0.853\ \Omega = 1.0\ \text{p.u.} \tag{26}$$

To determine $N_{ph}$, an arbitrary number of coil phase turns $N_{ph(\text{i})}$ together with currents $I_d = I_{d(\text{rated})}$ and $I_f = I_q = 0$ are used in a single nonlinear static FEA solution of the SC to determine $\lambda_{di}$ and $X_{di}$. From this, the phase turns are updated by

$$N_{ph(\text{i}+1)} = \sqrt{\frac{\lambda_{d(\text{rated})}}{\lambda_{di}}} N_{ph(\text{i})} = \sqrt{\frac{X_d}{X_{di}}} N_{ph(\text{i})}. \tag{27}$$

The phase turns can then be determined iteratively by (27) or it can be determined from an interpolating polynomial using FEA flux linkage data for some arbitrary turns as in [11]. Obviously, $N_{ph}$ must be rounded-off to the nearest integer.

### *B. Determining the No-Load Field Current $I_{f\text{-}NL}$*

The next step is to determine the operating V-curve of the SC, which is determined according to Fig. 1 by the field current region $0 \leq I_f \leq 2.0$ p.u. Hence, we must determine the base value per unit field current of the SC, which is also classically the no-load field current, i.e., $I_{f\text{-}NL} = I_f = 1.0$ p.u. The rated field current according to Fig. 1 is then $I_{f(\text{rated})} = 2I_{f\text{-}NL} = 2.0$ p.u.

In Fig. 1 at $I_f = 1.0$ p.u, $I_d = I_q = 0$ and the induced voltage of the SC is equal to the grid voltage, which in this case is 16 kV line-to-line according to (24). From (6), we have then

$$E_{df} = \sqrt{\frac{2}{3}} V_L = 13.06 \text{ kV}. \tag{28}$$

In the same way as above for the phase turns, $I_{f\text{-}NL}$ can be determined by iteratively updating

$$I_{f(\text{i}+1)} = \frac{E_{df}}{E_{di(\text{i})}} I_{f(\text{i})} \tag{29}$$

or by using the interpolating polynomial approach of [11].

## V. Grid-Tied Performance Simulation Method

The performance calculation of the SC in Section III is based on that the currents of the grid-connected SC are solved for a certain given field current. In this section, it is shown how this is done by means of static FEA and using the frozen permeability (FP) technique.

### *A. Determining the Reactance Matrix Vector*

Given the *dq* and field current of the SC, the reactance and field induced voltages of (5) and (6) must be determined. For this, we use (1) and (2) expressed in terms of voltages as

$$\omega_e \begin{bmatrix} \lambda_d \\ \lambda_q \end{bmatrix} = \begin{bmatrix} X_d & X_{dq} \\ X_{qd} & X_q \end{bmatrix} \begin{bmatrix} I_d \\ I_q \end{bmatrix} + \begin{bmatrix} X_{df} \\ X_{qf} \end{bmatrix} I_f. \tag{30}$$

Running a static *nonlinear* FEA solution of the SC for the given current vector $\mathbf{I} = [I_d\ I_q\ I_f]^{\text{T}}$, the permeabilities of the mesh elements are saved or frozen. With these frozen element permeabilities, three *linear* static FEA solutions are run for three current vectors $[I_d\, 00]^{\text{T}}$, $[0\, I_q\, 0]^{\text{T}}$, and $[00\, I_f]^{\text{T}}$, from which three sets of *dq* flux linkages are used to determine the parameters of (30) as follows:

$$\begin{bmatrix} X_d \\ X_{qd} \end{bmatrix} = \begin{bmatrix} \lambda_d \\ \lambda_q \end{bmatrix} \frac{\omega_e}{I_d}; \quad \begin{bmatrix} X_q \\ X_{dq} \end{bmatrix} = \begin{bmatrix} \lambda_q \\ \lambda_d \end{bmatrix} \frac{\omega_e}{I_q}; \quad \begin{bmatrix} X_{df} \\ X_{qf} \end{bmatrix} = \begin{bmatrix} \lambda_d \\ \lambda_q \end{bmatrix} \frac{\omega_e}{I_f}. \tag{31}$$

We define a reactance matrix vector $\mathbf{U}$ that contains the information of (31) as

$$\mathbf{U} = [X_d\ X_q\ X_{dq}\ X_{qd}\ X_{df}\ X_{qf}]^{\text{T}}. \tag{32}$$

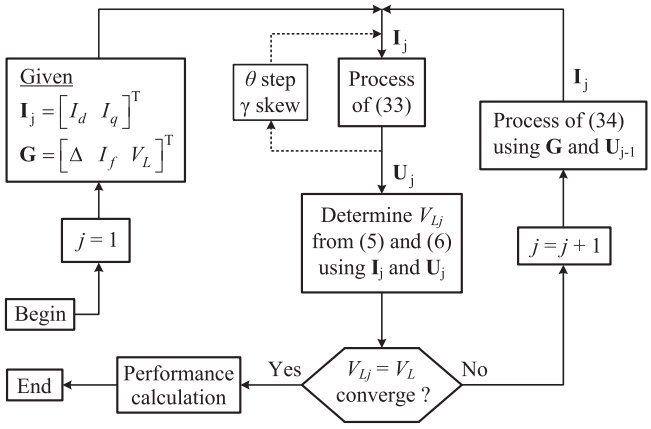


Fig. 3. Flow diagram for solving *dq* currents of the SC.

The above process is described by the following flow diagram, the so-called FP technique

$$\mathbf{I} \rightarrow \boxed{\begin{array}{c}\text{Non}-\text{linear} \\ \text{FEA solution}\end{array}} \rightarrow \boxed{\begin{array}{c}\text{Determine} \\ \text{parameters by} \\ \text{FP linear FEA} \\ \text{and (31)}\end{array}} \rightarrow \mathbf{U}. \tag{33}$$

### *B. Determining the Currents*

With the reactance parameters known from (32), as well as the phase resistance $R_s$, we can solve analytically *dq* currents of the SC for the given line voltage $V_L$, power angle $\Delta$, and field current $I_f$ from (5) and (6) expressed as

$$\text{Given} \rightarrow \begin{bmatrix} \Delta \\ I_f \\ V_L \end{bmatrix} \rightarrow \boxed{\begin{array}{c}\text{Solve analytically} \\ \text{from (5) and (6)} \\ \text{using } \mathbf{U} \text{ of (32)}\end{array}} \Rightarrow \begin{bmatrix} I_d \\ I_q \end{bmatrix}. \tag{34}$$

Note that in (5) and (6) the induced field voltages are given by (30) as $E_{df} = X_{df} I_f$ and $E_{qf} = X_{qf} I_f$.

To finally solve *dq* currents of the SC, we use the iterative process of Fig. 3. In this process, the *dq* currents of the SC is solved for given $V_L$, $\Delta$, and $I_f$. The field current $I_f$ is selected according to where in the V-curve operating region of Fig. 1 performance calculation of the SC is required. The value of the power angle $\Delta$ is explained in the following section.

The first step in the process of Fig. 3 is to run a nonlinear FEA solution for a given current vector $\mathbf{I}_j$; the latter can be an initial current vector chosen or from a previous solution. This is followed by determining $\mathbf{U}_j$ of (32) by the process of (33). With $\mathbf{I}_j$ and $\mathbf{U}_j$ known, $V_{Lj}$ is determined from (5) or (6) and compared with the grid voltage $V_L$ of (24) to test for convergence. If not, the process is repeated with the calculation of a new current according to (34) as shown in Fig. 3.

### *C. Determining the Power Angle $\Delta$*

To determine the very small power angle $\Delta$ of the SC, we follow here an approximation. For a given field current $I_f$, we first determine the *dq* currents of the SC according to the process

of Fig. 3 with the power angle set to $\Delta = 0$, that is

$$\text{Given} \rightarrow \begin{bmatrix} \Delta = 0 \\ I_f \\ V_L \end{bmatrix} \rightarrow \boxed{\begin{array}{|c|}\hline \text{Solve by} \\ \text{the process} \\ \text{of Fig.3} \\ \hline \end{array}} \Rightarrow \begin{bmatrix} I_d \\ I_q \end{bmatrix}. \tag{35}$$

From this, the reactance and induced voltages of (5) and (6) are all known from the FP FEA. As $\Delta$ is very small for the SC, the solved currents of (35) are very close to the actual *dq* currents and hence the reactance and induced voltages of (5) and (6) are very close to their actual values. To simplify further, we ignore the terms in brackets in (5) and (6), hence we can express the rotational losses using the classical *dq* power equation in motor operation as

$$\begin{aligned} P_{ROT} &= -\sqrt{\frac{3}{2}}\frac{E_{df}V_L}{X_d}\sin\Delta - \frac{V_L^2(X_d - X_q)}{2X_dX_q}\sin 2\Delta \\ &= -A\sin\Delta - B\sin 2\Delta \\ &\approx -(A + 2B)\Delta \end{aligned} \tag{36}$$

since $\Delta$ is small. The power of (36) is positive hence $\Delta$ is negative, which is correct for motor operation. With FEA flux density data available from the solution of (35), the rotational losses $P_{ROT}$ in (36) can be determined from (11), (12), and (15). With $P_{ROT}$ and the factors *A* and *B* known, $\Delta$ can be solved from (36). This $\Delta$ is then assumed as the correct power angle of the SC and used in the solution of the *dq* currents.

### D. Rotor Stepping and Skewing

At this stage of the grid-tied SC performance simulation, the SC is analyzed and solved at one rotor position. For multiple rotor positions $\theta_{n,}$ the process of (33) is done for all the rotor positions as shown in dotted lines in Fig. 3. Note that every time (33) is executed, the voltage vector amplitude $v_{s(\theta)}$ of (19) is determined as well as the position torque $\tau_{e(\theta)}$ from the Maxwell stress tensor method. For *n* positions, the reactance vector of (32) and Fig. 3 is determined as

$$\mathbf{U}_{\mathrm{j}} = \frac{1}{n}\sum_{n}\mathbf{U}_{\mathrm{n}}. \tag{37}$$

To reduce the torque ripple of the SC, the rotor is among other things skewed. To incorporate skewing in the solution of the *dq* currents of the SC, we implement the multislice model method. In this method, the rotor is divided axially in rotor stack slices *m* of which each slice is rotationally displaced by a skew angle $\gamma$ given by

$$\gamma = \frac{\theta_{sk}(2i - m - 1)}{2i} \quad [i = 1,\, 2,\, \ldots\, , m] \tag{38}$$

where

$$\theta_{sk} = k\frac{2\pi}{N_s} \quad [0 \le k \le 2] \tag{39}$$

and where $k$ represents the amount of skew. Again, position stepping (33) is executed for all the skewed stack slices and at all the rotor positions as indicated in Fig. 3. From this, the reactance vector of (32) and Fig. 3 is determined for *m* slices and *n* positions as

$$\mathbf{U}_{\mathrm{j}} = \frac{1}{n\,m}\sum_{n}\sum_{m}\mathbf{U}_{\mathrm{mn}}. \tag{40}$$

Note for the skewed case, the voltage vector amplitude $v_{s(\theta)}$ of (19) and the position Maxwell stress tensor torque $\tau_{e(\theta)}$ is determined at rotor position $\theta$ as

$$v_{s(\theta)} = \frac{1}{m}\sum_{m} v_{sm\,(\theta)}\,; \quad \tau_{e(\theta)} = \frac{1}{m}\sum_{m}\tau_{em\,(\theta)}. \tag{41}$$

When convergence is reached as shown in Fig. 3, the final performance calculation of the SC is done according to the formulations of Section III.

The process of Fig. 3 seems to be very time consuming, however the solution of the new currents is very close to the solved currents of the previous simulation, so that the number of iterations *j* is in general low. Convergence of the calculation flow diagram of Fig. 3 is typically reached with $j = 3$.

## VI. Design Optimization

SCs are known to be extremely large; hence, they can pose manufacturing, economic, and logistic challenges. For optimum performance, the adopted cooling measure, which can be expressed in terms of dissipated losses (16), is critical [2]. Although, SCs primarily supply reactive power, a small active power is also present to cater for the losses. Hence, due to this negligible amount of active power, torque ripple (21), very close to the cogging torque, can occur in them, which lead to unnecessary vibrations, as well as long-term wear and tear.

Power quality is also a very important factor to consider in the operation of SCs given that they are connected to the constant-voltage electric grid when operational. Thus, the percent total harmonic distortion, say for voltage (20), is a very critical factor to emphasize due to certain prescribed limits on bus voltages at the point of interconnection [17]. Therefore, for the proposed turbo SC design, a global optimization has been undertaken to minimize both total mass and total losses from the CM of WF-FSM SC.

The global optimization problem is set up as follows:

$$F\,(\ddot{x}) = \begin{bmatrix} M_A \\ P_{loss} \end{bmatrix}; \;\; -350 \;\le Q \le -300 \text{ MVAR} \tag{42}$$

where $\ddot{x}$ contains nine design variables made up mostly of dimensional parameters expressed in [11], *F* is the objective function comprising $M_A$ and $P_{loss}$, both representing total active mass and total losses, respectively, while *Q* is constrained as shown. Above and beyond, the stator outer diameter was kept constant at 9.5 m during the optimization process.

The workflow of the optimization process is illustrated in Fig. 4, where the 2-D FEA calculation is based on the process summarized in Fig. 3 through (33), and performed at the rated operating point $I_f = 2I_{f\text{-}NL}$. After 50 generations, the optimization process converges, meeting all the optimum requirements. An optimum benchmark, "GOM," is then selected from a pool of optimum design candidates, to further evaluate the performance of the proposed turbo WF-FSM SC. The resolved optimum

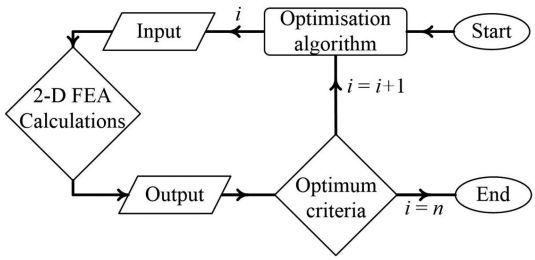


Fig. 4. Depiction of the FEA-based design optimization workflow ($i$ is iteration number, $n$ is number of generations).

TABLE II
EVOLVED OPTIMUM DESIGN PARAMETERS OF GOM SC

| Parameters | Values |
|---|---|
| Stator inner diameter, $D_i$ | 7.99 m |
| Stack length, $l_{st}$ | 6.66 m |
| Stator yoke width, $h_{ys}$ | 430 mm |
| Stator slot opening, $b_{sls}$ | 353 mm |
| Rotor pole width, $b_{pr}$ | 762 mm |
| Rotor yoke width, $h_{yr}$ | 676 mm |
| Airgap length, $g$ | 18 mm |
| Shaft diameter, $D_{sh}$ | 4.5 m |
| Phase winding turns, $N_{ph}$ | 2 turns |
| Field winding turns, $N_f$ | 6 turns |
| Phase winding current density, $J_{ph}$ | 0.65 A/mm$^2$ |
| Field winding current density, $J_f$ | 1.94 A/mm$^2$ |

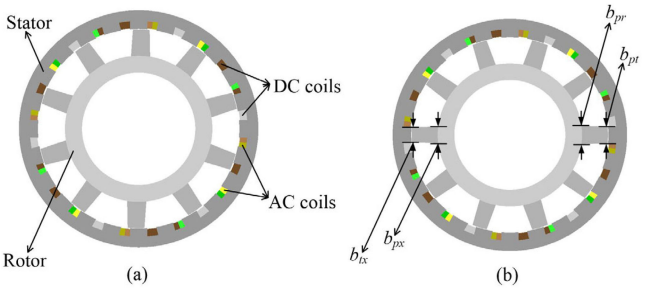


Fig. 5. Cross-sectional layout of the designed GOM SC. (a) Without pole-pairing. (b) With 0.9 pole-pairing ratio.

design parameters of GOM are presented in Table II and the cross-sectional layout of GOM is shown in Fig. 5(a).

## VII. 3-D FEA EVALUATION

To independently verify the prediction of the proposed turbo WF-FSM SC, since it is not possible for us to build and test an experimental prototype of that scale, a 3-D model of GOM is designed and transient FEA simulations performed in steady state. The obtained results, which among other things elucidate the end-winding effects, are discussed in this section.

The 3-D model is built using the commercial FEA package, ANSYS Maxwell. The flux density map of the modeled machine at $I_f = 2I_{f\text{-}NL}$ is mirrored as shown in Fig. 6. It is seen that the cores are not saturated beyond 2.4 T, which is an indication of good overload capacity. The flux density is also very much

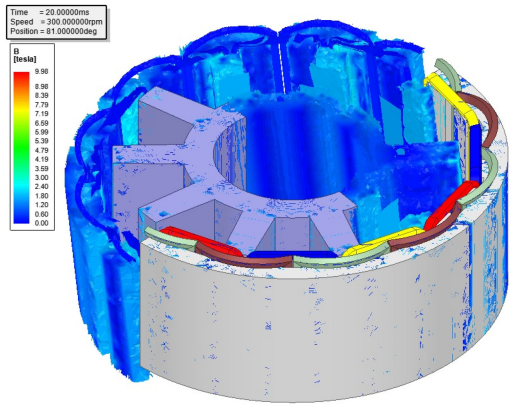


Fig. 6. 3D display of flux density on the GOM designed SC.

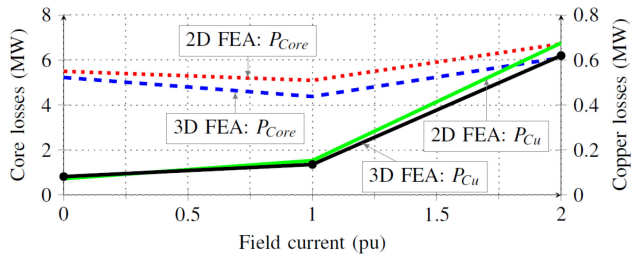


Fig. 7. Calculated losses in 2-D and 3-D FEA of the GOM designed SC.

TABLE III
2-D VERSUS 3-D FEA PERFORMANCE COMPARISON FOR GOM SC AT $I_f = 2$ P.U.

| Parameters | FEA | |
|---|---|---|
| | 2D | 3D |
| Input power, $P$ (MW) | 0.13 | 0.14 |
| Reactive power, $Q$ (MVAR) | −275.6 | −275.5 |

within the permitted loading levels, which should cater for appropriate design of cooling and insulation [23].

In Fig. 7, the losses calculated in 2-D FEA are compared with those obtained in 3-D FEA for GOM. It is observed that the results conform to a great extent, especially in terms of $P_{Cu}$. Moreover, the accuracy of the end-winding inductance is also checked and confirmed by comparing the reactive power generation at the critical operating point ($I_f = 2I_{f\text{-}NL}$), as shown in Table III. Clearly, the discrepancy between the 2-D and 3-D FEA predictions is not out of proportions. Overall, the 3-D FEA results validate the performance of designed turbo SC while downsizing any discrepancy that might result due to end-winding effects.

## VIII. MINIMIZING TORQUE RIPPLE

It is well known that the WF-FSM can have high torque ripple, which is not conducive in large machines such as the considered 300 MVAR SC in this article. The average torque of the WF-FSM SC is basically zero, but the torque ripple can be very high, which should be minimized in the design of the SC. We therefore pay

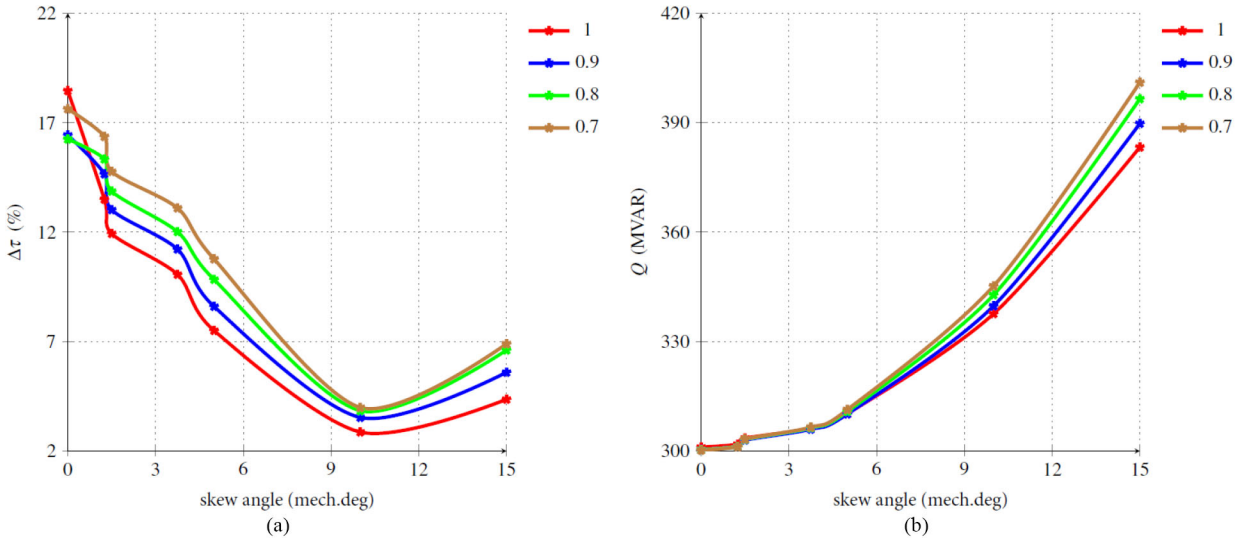


Fig. 8. Variation of skew angle and rotor pole-pairing parameter at $I_f = 0$ for (a) percentage torque ripple, and (b) reactive power.

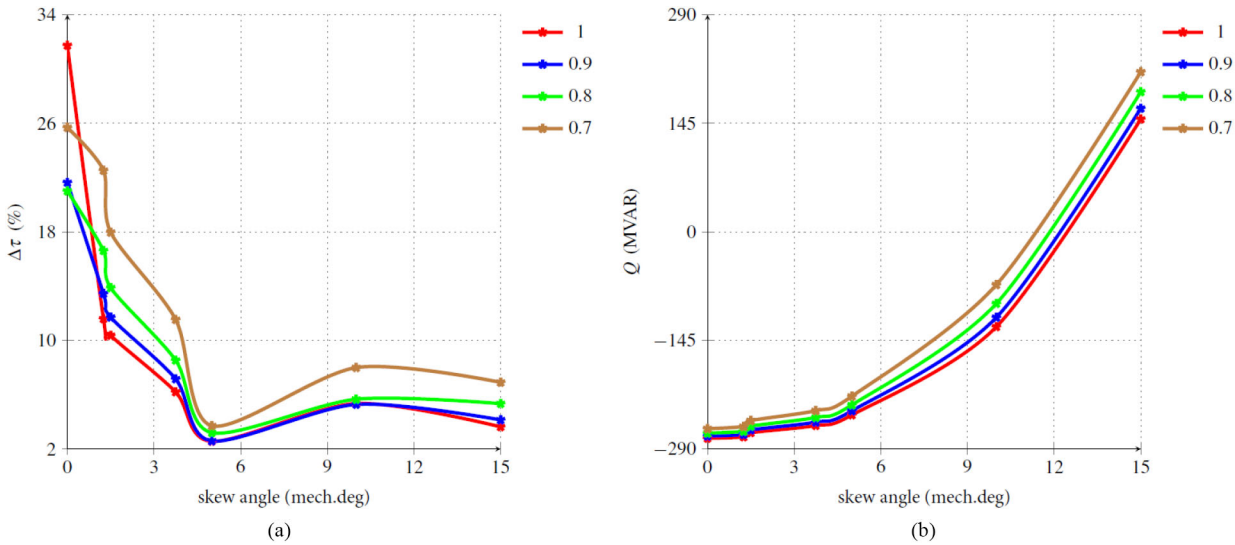


Fig. 9. Variation of skew angle and rotor pole-pairing parameter at $I_f = 2.0$ p.u. for (a) percentage torque ripple, and (b) reactive power.

special attention to this aspect in this section. The torque ripple is calculated according to (21).

To reduce the torque ripple of the turbo SC, rotor-skewing and pole-pairing techniques are applied. The rotor skewing is inspired from the study in [24], while the rotor pole-pairing from [25]. The rotor step skewing in [24] has been adjudicated as a simple and cost-effective technique for reducing cogging torque and torque ripple in flux switching machines. It was found in [25] that when the pole-pairing ratio is 0.8 for a small dc variable flux machine (DC-VRM), the torque ripple is reduced drastically with minimum effect on the average torque.

The currents of the skewed rotor SC are solved by means of the method explained in Section V-B. The amount of skewing applied in the FEA model is measured in terms of half a slot pitch, which is 15° mechanical. The skewing angles are thus varied between 0° and 15°. For the rotor pole-pairing technique, the adjacent rotor pole widths are adjusted according to the ratios $b_{tx}$:$b_{pt}$ and $b_{px}$:$b_{pr}$ as illustrated in Fig. 5(b).

The effect of the amount of skewing and rotor pole-pairing on the torque ripple and the reactive power of the SC are shown in Figs. 8 and 9, respectively, for $I_f = 0$ and $I_f = 2.0$ p.u. Since the main objective is to minimize torque ripple, with $I_f = 0$, a minimum torque ripple of 2.9% is obtained at a skew angle of 10° and a pole-paring ratio of 1. On the other hand, when $I_f =$ 2.0 p.u., a minimum torque ripple of 2.6% is obtained at a skew angle of 5° and again a pole-paring ratio of 1. Unlike what is reported in [25], it appears thus from Figs. 8(a) and 9(a) that rotor pole-pairing plays a little role in addressing torque ripple for the benchmark machine considered in the study at turbo range.

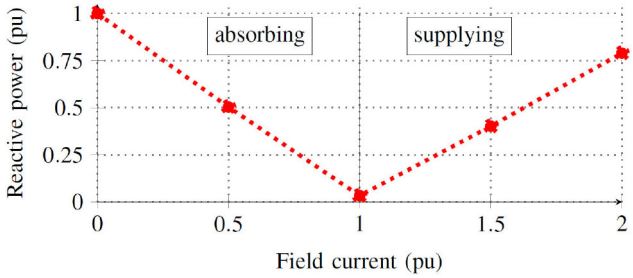


Fig. 10. Per unit reactive power V-curve of the SC.

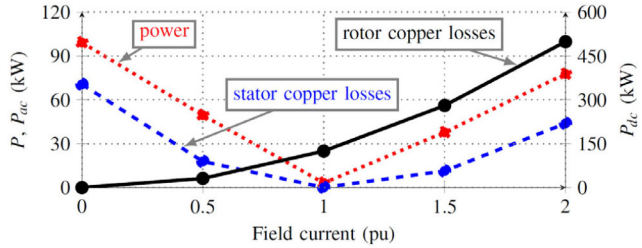


Fig. 11. Input power ($P$) and copper losses ($P_{ac}$ and $P_{dc}$) of the SC versus per unit field current.

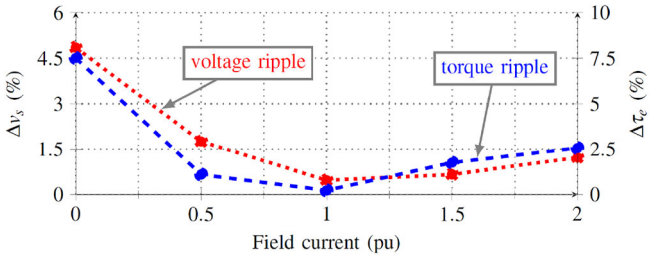


Fig. 12. Percentage voltage quality and torque ripple versus per unit field current at 5° rotor skew angle.

Considering the effect on reactive power, it is clear from Figs. 8 and 9 that skewing worsens the imbalance in the capable absorbing and supplying reactive power of the SC, respectively. With $I_f = 0$, skewing increases the capable absorbing reactive power due to significant decrease in the $d$-axis reactance, with consequent increase in stator current [see (8)]. With $I_f = 2$ p.u., however, skewing decreases the supplying reactive power due to significant decrease in the $d$-axis and field-coupling reactance with consequent decrease in stator current. Without pole pairing, optimum skewing of 10° according to Fig. 8(a) causes a 54% decrease in capable supplying reactive power [see Fig. 9(b)], but only a 12% increase in capable absorbing reactive power [see Fig. 8(b)]. However, with an optimum skew of 5° according to Fig. 9(a), there is only 11% decrease in capable supplying reactive power [see Fig. 9(b)] and 3% increase in capable absorbing reactive power [see Fig. 8(b)].

From the abovementioned, we thus opted for a 5° skew angle and a pole-pairing ratio of 1 (no pole-pairing) going forward. These have been chosen specifically to not impair the supplying reactive power at $I_f = 2$ p.u. too much, which is the critical SC operating point. In the next section, the turbo SC performance evaluation is thus undertaken for the selected design candidate.

## IX. Simulated Performance Results

In this section, we consider some simulated performance results across the whole V-curve operating region of the designed SC of Table II with its combined optimum pole-paired and skewed rotor. The performance calculations are done by the calculation methods explained in Sections V and VIII.

### A. Current and Power Results

With the skewed rotor SC connected to 16-kV supply voltage, the ac phase current and field current are numerically solved. It is found that the current densities on the ac and dc windings are in very low range for moderate cooling [23].

The most important result of the WF-FSM SC is the reactive power V-curve shown in Fig. 10. This shows that close to rated supplying reactive power is obtained, the effect of skewing is clear by a reduced supply reactive power capability at 2.0 p.u. field current, among other things. The latter tendency of a lower supply reactive capability is common in the SC operation [4]. Nevertheless, a wide range of reactive power regulation (+310.2/–244.6 MVAR) is exhibited, with possibility of operating without field current, just as for high temperature superconducting SCs [2].

In Fig. 11, the supply power and some power losses versus field current are shown. Recall that the core losses have been confirmed by transient FEA using the commercial ANSYS Maxwell package in Fig. 7. As expected, $P_{Cu} = P_{ac} + P_{dc}$ increases with $I_f$. Between them, $P_{Core}$ is the dominant loss and upon which the thermal burden of the SC rests on.

### B. Voltage and Torque Quality

The percentage voltage quality and torque ripple versus field current are shown in Fig. 12. This confirms a very low percentage torque ripple throughout the evaluated field current range and thus through the main operating points of the SC. Also, the percentage voltage quality is within specifications throughout the SC operating regime. Fig. 13 shows the actual voltage and torque waveforms of the SC at 2.0 p.u. field current. These results are promising for the use of a WF-FSM as turbo SC in terms of grid-connection and mechanical noise.

### C. Induced Voltage and Reactance Results

In Fig. 14, the per unit field induced voltages across the operating region of the SC are shown. This shows the expected linear relationship between the field current and the $d$-axis induced voltage $E_{df}$ due to the fixed terminal voltage, and hence, very much fixed saturation levels. The $q$-axis induced field voltage $E_{qf}$ as shown in Fig. 14 can be ignored in the analysis. The latter is not unexpected as the flux operation of the SC for all practical purposes occurs only on the $d$-axis.

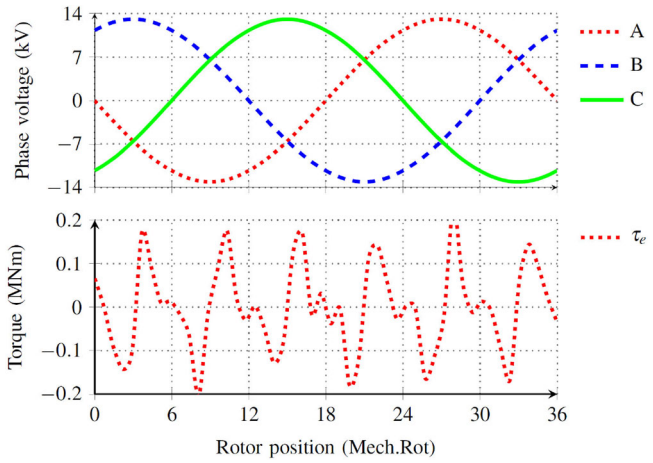


Fig. 13. Phase voltage and torque waveforms of the SC at $I_f = 2.0$ p.u. at 5° rotor skew angle.

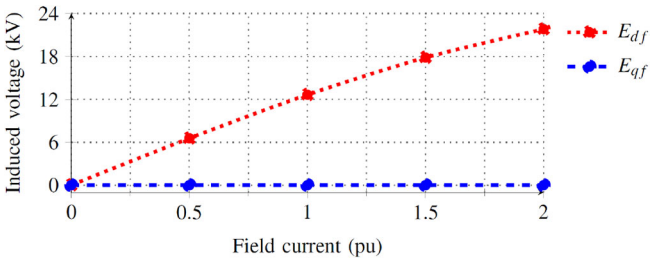


Fig. 14. Induced voltages $E_{df}$ and $E_{qf}$ versus per unit field current 300 r/min.

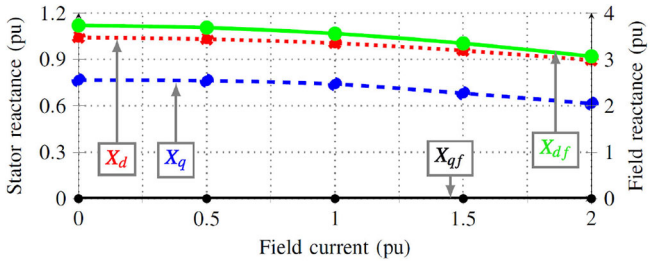


Fig. 15. DQ and field reactance effects under varying field current.

One of the important results of this study is the per unit *dq* and mutual reactance of the grid-tied WF-FSM SC as shown in Fig. 15. These results show that $X_d$ reactance is just less than 1.0 p.u., which fits perfectly with grid connection. There is also a slight saliency difference between $X_d$ and $X_q$. The cross-coupling reactance $X_{dq}$ is not shown since it can be ignored in the analysis of the SC for the same reason as earlier mentioned for ignoring the $q$-axis field induced voltage.

### D. Specific Performance of SC

We summarize the performance specifications of the proposed WF-FSM SC in Table IV at two extreme operating points of the SC namely at $I_f = 0$ p.u. and $I_f = 2.0$ p.u. In Table IV, an additional performance parameter is highlighted namely, the inertia constant $H$ of the SC at 14 s. With the WF-FSM SC

TABLE IV
SPECIFIC PERFORMANCE PARAMETERS OF THE SC 5° SKEWING ANGLE

| Parameters | $I_f = 0$ pu | $I_f = 2.0$ pu |
|---|---|---|
| Reactive power, $Q$ | 310.2 MVAR | –244.6 MVAR |
| Line voltage, $V_L$ | 16 kV | 16 kV |
| Total loss, $P_{loss}$ | 5.81 MW | 9.47 MW |
| Field current, $I_f$ | 0 | 8.34 kA |
| $d$-axis current, $I_d$ | 15.83 kA | –12.48 kA |
| $q$-axis current, $I_q$ | 5.11 A | –4.3 A |
| Voltage ripple, $\Delta v_s$ | 4.85 % | 1.22 % |
| Torque ripple, $\Delta\tau_e$ | 7.51 % | 2.56 % |
| $d$-axis reactance, $X_d$ | 1.0 pu | 0.89 pu |
| $q$-axis reactance, $X_q$ | 0.77 pu | 0.62 pu |
| Phase angle, $\phi$ | 89.98° lagging | 89.98° lagging |
| Load angle, $\Delta$ | 2.25 ° | 0.7 ° |
| Total mass, $M_A$ | 1900 tons | |
| Inertia constant, $H$ | 14 s | |
| Split ratio ($D_i$:$D_o$) | 0.84 | |
| Aspect ratio ($l_{st}$:$D_i$) | 0.83 | |

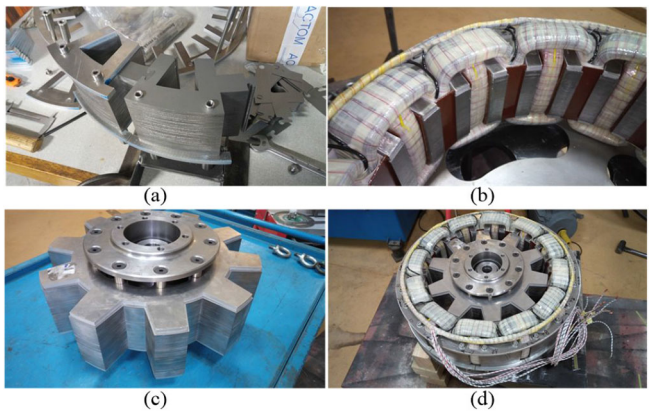


Fig. 16. Manufacturing and assembling: (a) stacking of stator laminations, (b) assembled coils, (c) assembled rotor, and (d) WF-FSM prototype.

operating speed at 300 r/min, which is much lower than those of the conventional rotating SCs operating at around 1500 r/min [3], it is clear from (22) and (23) that a high split ratio coupled with the sheer size of the designed turbo SC, more than rotor speed, are responsible. It should also be noted that achieving $H = 10$ s is phenomenal because a typical range is 2–3 s, where it is previously only possible beyond this range by employing flywheels [4], [6]. That said, a significantly high $H$ value as obtained for the designed WF-FSM SC is an important resource in SCs, which is critical to the electric grid performance in terms of lowering ROCOF, as well as boosting of ride through capability [1], [3], [6].

## X. EXPERIMENTAL TESTS

This section reports on the measurements for SC operation carried out on an existing small-scale three-phase 12/10 WF-FSM prototype [26]. The manufactured prototype and experimental setup are shown in Figs. 16 and 17. The highlight of the experiment is the successful connection of the WF-FSM as SC directly to the grid, for the first time [27].

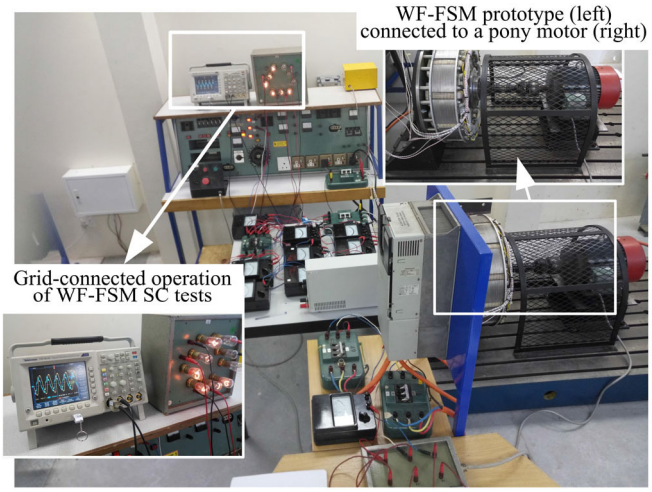


Fig. 17. Experimental test-bench of a small-scale WF-FSM SC prototype.

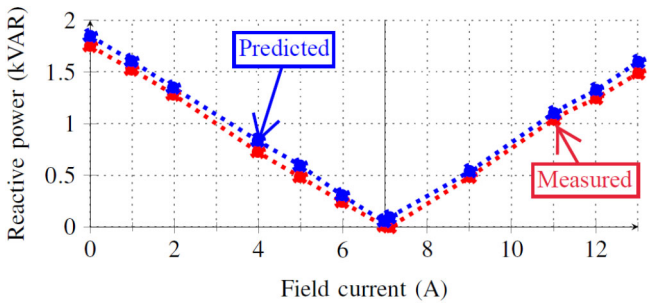


Fig. 18. V-curves for proposed FP FEA technique versus measurements.

The process is explained as follows: the machine is first brought up to speed for grid synchronization using a smaller induction machine which served as a pony motor. Thereafter, the latter was electrically isolated from the test machine and allowed to freewheel without posing further mechanical interference. The test machine is then gradually excited from 0 to a reference rated field current value of 7.1 A. At the rated field current, the machine was synchronized to the grid and locked to a line voltage of 280 V, 50 Hz. While on the grid, the field current is then varied between underexcited (0–7.1 A) and overexcited (7.1–13 A) modes. The relevant experimental performance data were captured, from which the V-curve of the prototype machine is produced as shown in Fig. 18. One can observe that the experimental setup is compared at par as per the proposed FEA FP iterative technique described in Fig. 3 and (33). Apart from minor discrepancy observed due to manufacturing defects, both curves clearly match.

It is important to note that in the SC operation the power factor is basically zero at the two extreme operating points, i.e., $I_f = 0$ and $I_f = 2.0$ p.u., as explained in Fig. 2. Should the power factor of the machine be unity, i.e., $I_f = 1$ p.u., then it ceases to act as SC, meaning there is no reactive power being absorbed nor supplied (see Figs. 1, 10, and 18). In summary, the WF-FSM SC functions as a variable inductor or capacitor.

## XI. Conclusion

In this study, an iterative FEA FP analytical procedure for the accurate performance prediction of turbo WF-FSM SCs is proposed. Based on a global optimum design benchmark, it is clearly shown that the standard V-curves that define the main operating points in SC performance can be easily acquired, with the line voltage profile constantly maintained to the grid specifications irrespective of the operating point. The torque ripple effects of the proposed SC technology, which can pose enormous design challenge is also carefully addressed by investigating on the simple rotor pole-pairing and skewing techniques. Based on the obtained results, the rotor pole-pairing technique is eventually disregarded as it seems not to address the issue of torque ripple in the turbo range of the proposed machine. In the end, the optimum torque ripple reduction is selected at 5° mechanical rotor skew angle, which yields 2.6% torque ripple at 11% drop in capable supplying reactive power at the field current operating point of $I_f$= 2.0 p.u.

In addition, it is found that the proposed SC machine can exhibit high inertia constant and less than unitary per unit reactance, which are representative of a robust and fault-tolerant performance on the electricity grid. Sequel to successful experimental validation of the proposed SC technology based on an existing small-scale prototype, the study not only proves to be potentially critical for the emerging industry, but it also provides a useful template for the general performance prediction of rotating SCs.

## Acknowledgment

The authors would like to thank Kenan Cloete and Andrew T. Loubser of the Electrical Machines Laboratory, Stellenbosch University, South Africa, for their support in the manufacturing and testing of the reported SC prototype.

## References

[1] P. E. Marken, A. C. Depoian, J. Skliutas, and M. Verrier, "Modern synchronous condenser performance considerations," in *Proc. IEEE Power Energy Soc. Gen. Meeting*, Detroit, MI, USA, 2011, pp. 1–5.

[2] L. Chubraeva and S. Timofeev, "Modern reactive power generators," in *Proc. IOP Conf. Ser. Mater. Sci. Eng.*, 2018, vol. 313, pp. 1–10.

[3] C. Szabo, "Synchronous condensers: An old tool rediscovered to address grid challenges," Power Eng. Int., News, pp. 6–8, Dec. 2017.

[4] J. P. Skliutas *et al.*, "Planning the future grid with synchronous condensers," in *Proc. CIGRE US Nat. Committee, Grid Future Symp.*, Paris, France, 2013, pp. 1–12.

[5] J. M. Fogarty and R. A. Nold, "Application of synchronous condensers in the modern power grid," CNY Eng., New York, NY, USA, 2017. [Online]. Available: http://www.cscos.com/wp-content/uploads/Electric2_JFogarty.pdf

[6] Y. Liu, S. Yang, S. Zhang, and F. Z. Peng, "Comparison of synchronous condenser and STATCOM for inertial response support," in *Proc. IEEE Energy Conv. Congr. Expo*, Pittsburgh, PA, USA, 2014, pp. 2684–2690.

[7] J. Jia, G. Yang, A. H. Nielsen, E. Muljadi, P. Weinreich-Jensen, and V. Gevorgian, "Synchronous condenser allocation for improving system short circuit ratio," in *Proc. 5th Internal Conf. Elect. Power Energy Convers. Syst.*, Kitakyushu, Japan, 2018, pp. 1–5.

[8] Z. Ling, Y. Cui, L. Ruan, W. Cai, Y. Zhang, and R. Yang, "The effect of load condition on dynamic response capability of synchronous condenser," in *Proc. 20th Int. Conf. Elect. Mach. Syst.*, Sydney, NSW, Australia, 2017, pp. 1–4.

[9] J. Zhou *et al.*, "A method of evaluating the stator inter-turn short circuit fault of synchronous condenser," in *Proc. 21st Int. Conf. Elect. Mach. Syst.*, Jeju, South Korea, 2018, pp. 520–524.
[10] T. Wildi, *Electrical Machines, Drives, and Power Systems*, 6th ed., Hoboken, NJ, USA: Prentice Hall, 1981.
[11] U. B. Akuru and M. J. Kamper, "A modest attempt on the electromagnetic design and performance prediction of turbo wound-field flux switching synchronous condensers," in *Proc. IEEE Energy Convers. Congr. Expo*, Baltimore, MD, USA, 2019, pp. 1782–1789.
[12] S. E. Rauch and L. J. Johnson, "Design principles of flux–switching alternators," *Trans. Amer. Inst. Elect. Eng. Part III Power App. Syst.*, vol. 74 no. 3, pp. 1261–1268, Jan. 1955.
[13] J. X. Shen and W. Z. Fei, "Permanent magnet flux switching machines—Topologies, analysis and optimization," in *Proc. 4th Int. Conf. Power Eng., Energy Elect. Drives*, Istanbul, Turkey, 2013, pp. 352–366.
[14] U. B. Akuru and M. J. Kamper, "Intriguing behavioral characteristics of rare-earth-free flux switching wind generators at small- and large-scale power levels," *IEEE Trans. Ind. Appl.*, vol. 54, no. 6, pp. 5772–5782, Nov./Dec. 2018.
[15] Z. Wu, Z. Zhu, C. Wang, J. Mipo, S. Personnaz, and P. Farah, "Analysis and reduction of on-load DC winding induced voltage in wound field switched flux machines," *IEEE Trans. Ind. Electron.*, vol. 67, no. 4, pp. 2655–2666, Apr. 2020.
[16] M. Mabhula, "Analysis and design optimisation of grid-connected wound-rotor synchronous and induction motors," Ph.D. dissertation, Elect. Electron. Eng., Stellenbosch Univ,Stellenbosch, South Africa, Dec. 2019.
[17] SEMFEM. Accessed on: May 29, 2021 [Online]. Available: www0.sun.ac.za/semfem/index.html
[18] T. M. Blooming and D. J. Carnovale, "Application of IEEE STD 519-1992 Harmonic limits," in *Proc. Conf. Rec. Annu. Pulp Paper Ind. Tech. Conf.*, Appleton, WI, USA, 2006, pp. 1–9.
[19] J. T. Chen and Z. Q. Zhu, "Winding configurations and optimal stator and rotor pole combination of flux-switching PM brushless AC machines," *IEEE Trans. Energy Convers.*, vol. 25, no. 2, pp. 293–302, Jun. 2010.
[20] M. Mabhula, U. B. Akuru, and M. J. Kamper "Cross-coupling inductance parameter estimation for more accurate performance evaluation of wound-field flux modulation machines," *Electronics*, vol. 9, 2020, Art. no. 1748.
[21] T. Fukami, H. Aoki, K. Shima, M. Momiyama, and M. Kawamura, "Assessment of core losses in a flux-modulating synchronous machine," *IEEE Trans Ind. Appl.*, vol. 48, no. 2, pp. 603–611, Mar./Apr. 2012.
[22] T. A. Lipo, *Introduction to AC Machine Design*. Hoboken, NJ, USA: IEEE Press-Wiley, 2017.
[23] J. Pyrhönen, T. Jokinen, and V. Hrabovcova, *Design of Rotating Electrical Machines*, 5th ed. Chichester, U.K.: Wiley, 2008.
[24] W. Fei, P. C. K. Luk, and J. Shen, "Torque analysis of permanent-magnet flux switching machines with rotor step skewing," *IEEE Trans. Magn.*, vol. 48, no. 10, pp. 2664–2673, Oct. 2012.
[25] U. B. Akuru, M. J. Kamper, and M. Mabhula, "Optimisation and design performance of a small-scale DC vernier reluctance machine for direct-drive wind generator drives," in *Proc. IEEE Energy Convers. Congr. Expo.*, Detroit, MI, USA, 2020, pp. 2965–2970.
[26] U. B. Akuru and M. J. Kamper, "Novel experimentation of a 10-kW geared medium-speed wound-field flux switching wind generator drive," in *Proc. IEEE Energy Convers. Congr. Expo*, Portland, OR, USA, 2018, pp. 6492–6498.
[27] C. Africa, U. B. Akuru, and M. J. Kamper, "Bringing back the synchronous compensator for the south africa power network–simulation and compensator technology," in *Proc. IEEE Southern Afr. Univ. Power Eng. Conf./Robot. Mechatronics/Pattern Recognit. Assoc. South Afr.,* Bloemfontein, South Africa, 2019, pp. 648–654.

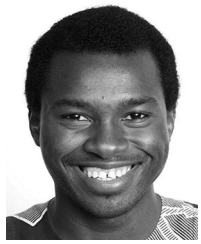

**Udochukwu B. Akuru** (Senior Member, IEEE) received the B.Eng. and M.Eng. degrees in electrical engineering from the University of Nigeria, Nsukka, in August 2008 and June 2013, respectively, and the Ph.D. degree in electrical engineering from Stellenbosch University, Stellenbosch, South Africa, in December 2017.

He is currently a Senior Lecturer with the Tshwane University of Technology, South Africa. Between 2018 and 2020, he was a Postdoctoral Research Fellow with Stellenbosch University. Since August 2011, he has also been with the University of Nigeria. He has authored or coauthored papers in various journals and conferences. His research interests mainly include electrical machines design and renewable energy technologies, with competency in finite element analyses and modeling of electrical machines.

Dr. Akuru is a registered Engineer with the Council for the regulation of Engineering in Nigeria (COREN), Senior Member of SAIEE, South Africa National Research Foundation (NRF) rated Researcher, Member of the Nigeria Young Academy (NYA), and volunteer of various societies, committees, and groups, such as the IEEE IAS EMC and IEEE IES EMTC. He is a Reviewer of IEEE conferences and transactions.

**Mkhululi Mabhula** (Member, IEEE) received the B.Eng. and Ph.D.Eng. – M.Sc. upgrade – degrees in electrical engineering from Stellenbosch University, South Africa in 2016 and 2019, respectively.

He is currently a Postdoctoral Research Fellow with Stellenbosch University. His research interests mainly include the design, optimization, and control of electrical machines.

**Maarten J. Kamper** (Senior Member, IEEE) received the M.Sc.Eng. and Ph.D. degrees in Electrical Engineering from the University of Stellenbosch, Stellenbosch, South Africa, in 1987 and 1996, respectively.

Since 1989, he has been with the Academic Staff, Department of Electrical and Electronic Engineering, University of Stellenbosch, where he is currently a Professor of electrical machines and drives. His research interests include computer-aided design and control of reluctance, permanent magnet, and inductance machine drives.

Prof. Kamper is a South African National Research Foundation (NRF) Rated Researcher and a registered Professional Engineer in South Africa.